

CLIMATOLOGY

Emergence of an equatorial mode of climate variability in the Indian Ocean

Pedro N. DiNezio^{1*}, Martin Puy¹, Kaustubh Thirumalai², Fei-Fei Jin³, Jessica E. Tierney²

Presently, the Indian Ocean (IO) resides in a climate state that prevents strong year-to-year climate variations. This may change under greenhouse warming, but the mechanisms remain uncertain, thus limiting our ability to predict future changes in climate extremes. Using climate model simulations, we uncover the emergence of a mode of climate variability capable of generating unprecedented sea surface temperature and rainfall fluctuations across the IO. This mode, which is inhibited under present-day conditions, becomes active in climate states with a shallow thermocline and vigorous upwelling, consistent with the predictions of continued greenhouse warming. These predictions are supported by modeling and proxy evidence of an active mode during glacial intervals that favored such a state. Because of its impact on hydrological variability, the emergence of such a mode would become a first-order source of climate-related risks for the densely populated IO rim.

INTRODUCTION

Predicting changes in the pattern and magnitude of sea surface temperature (SST) fluctuations over the tropical oceans is critical for attributing changing climate variability and extreme weather over large parts of the world (1). Observations show that the Indian Ocean (IO)—a tropical ocean long considered a minor driver of climate variability relative to the Pacific or the Atlantic oceans (2)—is experiencing changes in its mean state that could favor stronger SST variations (3–5). These long-term changes appear to be forced by increasing greenhouse gas (GHG) concentrations (5–7); however, models are inconclusive on whether SST variability will increase or not (8–12). Paleoclimate records show that SST variability in the eastern IO has increased since the 1850s (13), a trend that, if continued, could exacerbate the already sizable climatic impacts of subtle variations in IO temperatures over surrounding land masses (11, 14–17). While the changes in mean state—particularly a shoaling thermocline in the eastern IO—are likely to strengthen the coupled feedbacks governing SST variability (9–12), the lack of model consensus limits our ability to attribute the observed trends and predict future changes.

The tropical IO exhibits much weaker SST variability than the tropical Pacific and Atlantic oceans (Fig. 1A). Unlike these oceans, where the El Niño–Southern Oscillation (ENSO) phenomenon and the Atlantic Niño drive pronounced basin-wide SST anomalies (SSTAs), variability in the IO is restricted to the western side of the basin and along the coast of Sumatra and Java (18). Large SSTAs spanning the equatorial IO are extremely rare because the uniformly deep thermocline (Fig. 1B, shading) and a lack of equatorial upwelling (not shown) hinder coupled ocean-atmosphere interactions in this ocean (19). Depending on the season, the dominant mode of SST variability in the IO has a uniform warming pattern over the entire basin. This IO Basin (IOB) mode is not generated via ocean dynamical processes and instead is forced by El Niño events via changes in evaporation and cloud cover (20–23). The IO Dipole (IOD) is the

second mode of variability in terms of explained SST variance and has SSTAs restricted to the western IO and the off-equatorial region along the coast of Sumatra and Java (18). SSTAs driven by IOD events do not reach the equatorial IO, which only responds during very rare extreme cold events, such as during 1997 (11).

The intensity and spatial pattern of SST variations in the IO are thus determined by the direction of the prevailing winds along the equator, which are weakly westerly (Fig. 1C, vectors), and by the subtle east-west SST gradient underlying them (Fig. 1C, shading). Model simulations show that continued greenhouse warming could alter these features, and the IO could evolve into a mean state similar to the Pacific or Atlantic oceans (5, 7, 10). Historical observations support this prediction, showing a tendency for easterly winds along the equator, an eastward shoaling thermocline, and a reversal of the east-west SST gradient since the 1950s (3–6). These changes should be accompanied by increased SST variability along the equatorial IO (19); however, model predictions are not consistent with this theoretical expectation (8–11). Furthermore, the possibility that the IO could harbor stronger modes of climate variability has remained largely unexplored.

Here, we address these questions using numerical simulations of past and future climate changes in which the mean state of the IO could favor stronger variability. Our goal is to assess physical processes that could cause new modes of variability to emerge in the IO under continued greenhouse warming as well as the potential existence of these modes during past climate intervals. We analyze an ensemble of simulations of 21st-century climate performed by 36 models participating in the Coupled Model Intercomparison Project 5 (CMIP5). These simulations were run under increasing GHG concentrations following a “business as usual” high-emission scenario (see “Data” and “Methods” sections). These models accurately reproduce the observed patterns of variability in the southeastern IO (fig. S1) as well as long-term changes in the east-west gradient over the 1900–2017 period (fig. S2), lending credibility to their predictions of an altered mean state under continued greenhouse warming throughout the second half of the 21st century (see Supplementary Text 1 for additional model evaluation).

We also analyze simulations of the climate at the Last Glacial Maximum (LGM)—a past climatic interval ~21,000 years before present when the IO exhibited a similarly altered mean state featuring

Copyright © 2020
The Authors, some
rights reserved;
exclusive licensee
American Association
for the Advancement
of Science. No claim to
original U.S. Government
Works. Distributed
under a Creative
Commons Attribution
NonCommercial
License 4.0 (CC BY-NC).

¹Institute for Geophysics, Jackson School of Geosciences, University of Texas at Austin, J. J. Pickle Research Campus, Building 196, 10100 Burnet Road (R2200), Austin, TX 78758, USA. ²Department of Geosciences, The University of Arizona, 1040 E. 4th St., Tucson, AZ 85721, USA. ³Department of Atmospheric Sciences, University of Hawai'i at Manoa, 2525 Correa Road, Honolulu, HI 96822, USA.

*Corresponding author. Email: pdn@ig.utexas.edu

Modern climate of the tropical oceans

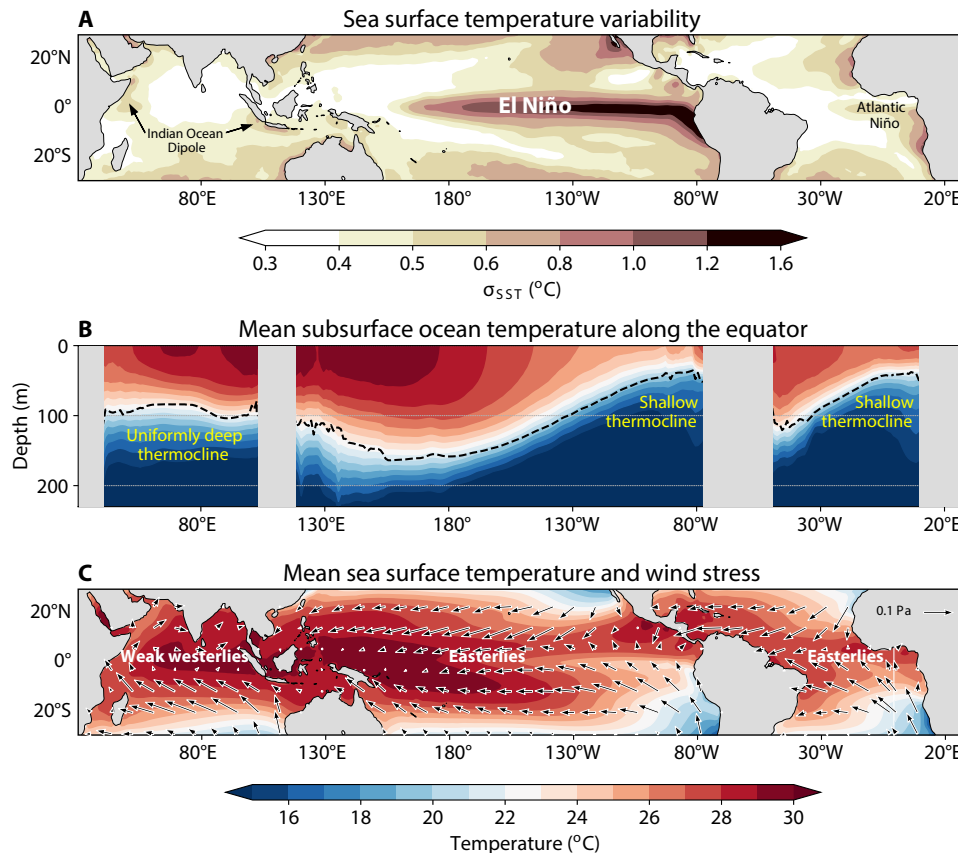


Fig. 1. Observed variability and mean state over the tropical oceans. (A) SST variability, (B) annual mean subsurface ocean temperature along the equator (5°S to 5°N), and (C) annual mean SST (shading) and surface wind stress (vectors). SST variability is computed as the SD of monthly anomalies relative to the monthly mean seasonal cycle. In the tropical oceans, a metric of variability that is dominated by variations occurring on interannual time scales. SST and surface wind stress are from TropFlux (46) and subsurface ocean temperature data are from ORAS-S4 (37).

stronger upwelling and an eastward shoaling thermocline (24, 25). The LGM simulations were performed with the Community Earth System Model version 1.2 (CESM1) (26), a model that simulates changes in IO mean state supported by multiproxy syntheses from this climate interval (24) and consistent changes in variability (27). To our knowledge, CESM1 is one of the very few climate models capable of simulating physical processes in the IO amplifying regional climate changes during the LGM (24), justifying the use of a single model for this part of our study. Despite being triggered by exposure of continental shelves due to lower glacial sea level (28), these changes result in changes in IO mean state and variability (24, 25, 27) analogous to those simulated under greenhouse warming, albeit in a globally colder climate. Additional CESM1 LGM simulations are used to isolate changes associated with both emergent and existing modes (Materials and Methods).

RESULTS

Our simulations indicate that under greenhouse warming and LGM conditions, the IO can exhibit increased SST variability in the eastern equatorial IO (EEIO) (Fig. 2, A and B). This pattern of intensification resembles modern variability in the other tropical oceans and represents a pronounced departure from current variability in the

IO, which is minimal along the equator (Fig. 1A). The increase in gSST variability occurs during late boreal summer (August–September–October) following changes in the mean state favoring stronger coupled interactions during the preceding months. Increased equatorial upwelling and an eastward shoaling thermocline during July–August–September (JAS) (Fig. 2, C and D) favor the development of SSTAs in the EEIO. The changes in mean state are also part of a coupled ocean–atmosphere response. Equatorial winds become more easterly under greenhouse warming and glacial conditions (Fig. 2, E and F, vectors), a response that is reinforced by the changes in the underlying SST gradient (Fig. 2, E and F, shading) via the cooling effect of a shallower thermocline. These coupled responses are initiated by different atmospheric processes: a reversal of westerly winds over the eastern IO driven by a weaker Walker circulation, for greenhouse warming (7); and an atmospheric response to shelf exposure, for the LGM (28). Despite the different triggering mechanisms, the same coupled feedbacks amplify the changes in both cases, generating an oceanic mean state reminiscent of the eastern equatorial Pacific and Atlantic oceans, with a shallow equatorial thermocline and vigorous upwelling favoring stronger air–sea interactions and SST variability (19).

The CMIP5 models show a direct link between the changes in mean climate and the increase in variability under greenhouse warming.

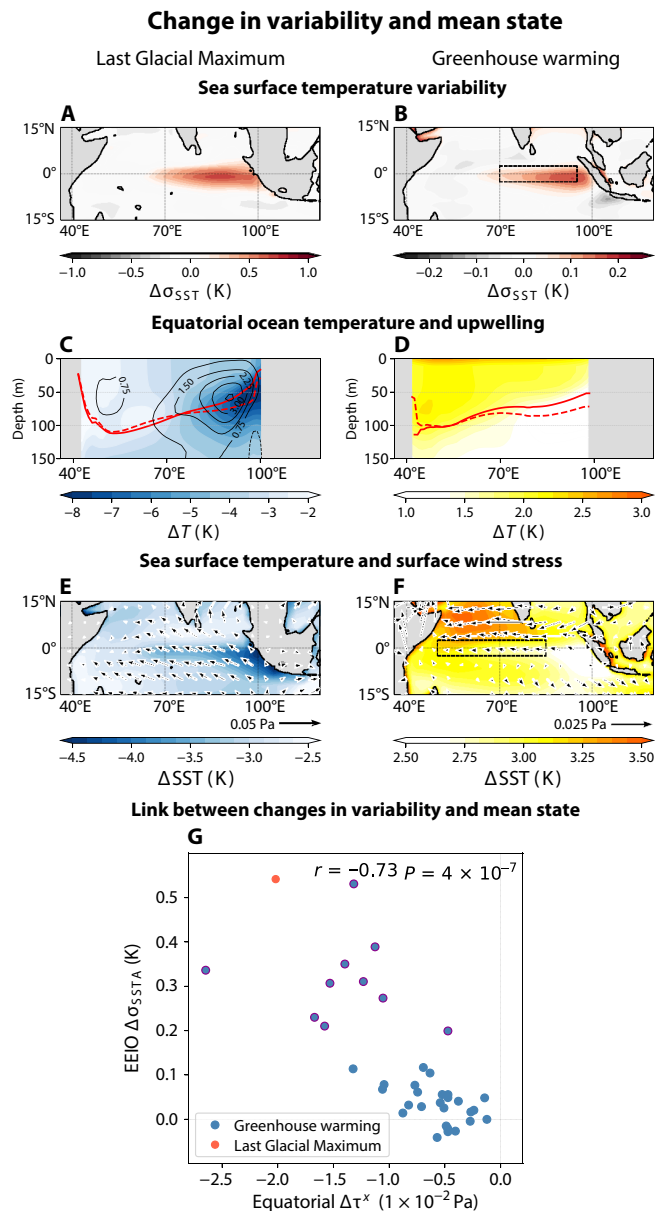


Fig. 2. Simulated changes in IO climate variability and mean state under glacial conditions and greenhouse warming. Changes in (A and B) SST variability, (C and D) subsurface ocean temperature (shading, m), vertical velocity (contours, m/day), and (E and F) SST (shading) and surface wind stress (vectors). Glacial changes (left) are computed from a simulation of LGM relative to a simulation of preindustrial (PI) climate, both performed with the CESM1. Changes under greenhouse warming are computed for the 2050–2100 interval in high-emission scenario [Representative Concentration Pathway 8.5 (RCP8.5)] simulations performed by 36 CMIP5 models relative to the 1850–1950 interval from historical simulations. The changes in variability are computed as the difference in SD of SSTAs during the August–September–October (ASO) season. Changes in mean state are computed for the JAS season. The changes under greenhouse warming are the average among the changes simulated among all 36 CMIP5 models. Dashed and solid red curves in (C) and (D) indicate the depth of thermocline in the reference (PI and historical) and altered (LGM and RCP8.5) climate states, respectively. (G) Relationship between changes in SD of SST anomalies in the EEIO (70°E to 95°E, 2.5°S to 2.5°N) during the ASO season and zonal wind stress in the equatorial IO (50°E to 80°E, 2.5°S to 2.5°N) during the JAS season for each model simulated response to greenhouse warming (blue circles) and LGM boundary conditions (red circle). Models with mode activation are outlined in red.

The magnitude of the increase in SST variability, measured by the change in SD of SSTAs averaged over the EEIO, is strongly anti-correlated with the changes in zonal wind stress along the equator ($r = -0.73$, $P < 0.001$; Fig. 2G). This indicates that greater easterly wind stress leads to a larger increase in variability, a relationship that reflects the influence of zonal winds on seasonal upwelling and thermocline depth over the EEIO. Most CMIP5 models predict increases in variability and more easterly winds for the second half of the century (Fig. 2G); however, the magnitude of these responses differs by an order of magnitude. Some CMIP5 models predict pronounced changes in equatorial winds accompanied by increases in SST variability of up to 100%. In these models, the magnitude of the changes represents a reversal of the climatological winds, i.e., absolute easterlies develop across the equatorial IO along with seasonally colder SSTs over the EEIO. A similar wind reversal and seasonal “cold tongue” is simulated under LGM conditions (not shown), resulting in the largest changes in variability among all simulations (Fig. 2G, red circle). These seasonal variations are similar to those occurring in the modern Pacific and Atlantic oceans, which sustain the ENSO and Atlantic Niño modes. Likewise, the simulated changes in the IO give rise to its own El Niño-like variability.

Under the altered mean states of the LGM and high-emission scenarios, climate variability in the IO manifests as warm and cold events that are physically different from those associated with the IOD—currently a dominant mode of IO climate variability (18, 29)—although superficially similar to very extreme IOD events. To isolate the dynamics of the emergent mode, we use our subset of LGM simulations in which ENSO and IOD modes are disabled (see “Methods” section). Results from these simulations show that events associated with the emergent mode are independent from the IOD (fig. S3) and, more importantly, that they are triggered by a distinct atmospheric precursor on the western IO (fig. S3A). Because additional simulations cannot be run with CMIP5 models, we isolate the events associated with the emergent mode using a methodology based on this wind precursor (fig. S4; also Materials and Methods). The CMIP5 simulations also show that these events are driven by a coupled mode that has not been observed in historical observations and could become active under continued greenhouse warming.

Unlike IOD events, which are triggered by wind fluctuations in the southeastern IO along the coast of Java and Sumatra (16, 30), events associated with the emergent mode are initiated remotely by an atmospheric circulation anomaly over the western IO and Arabian Sea (Fig. 3, left; vectors). This atmospheric precursor during late boreal spring and influences the EEIO via propagation of downwelling oceanic Kelvin waves along the equator (Fig. 3, left; contours). For warm events, the atmospheric precursor has a westerly wind stress anomaly along the equator that drives a Kelvin wave response characterized by a thermocline deepening toward the East (Fig. 3, A and C, contours). This response suppresses climatological cooling over the EEIO during late boreal summer, when the thermocline is seasonally shallower and upwelling is strong (Fig. 2, C and D), driving an initial warming in the EEIO. An anomalous zonal SST gradient is established along the equatorial IO, further weakening surface winds. These wind changes drive oceanic responses, thermocline deepening, and reduced upwelling that continue the warming of the EEIO until its peak during late boreal summer (Fig. 3, B and D, shading). Such coupled responses are akin to the positive feedback loop proposed by Bjerknes (31) for the growth of El Niño events in the Pacific Ocean.

Atmospheric precursor and activation of equatorial mode

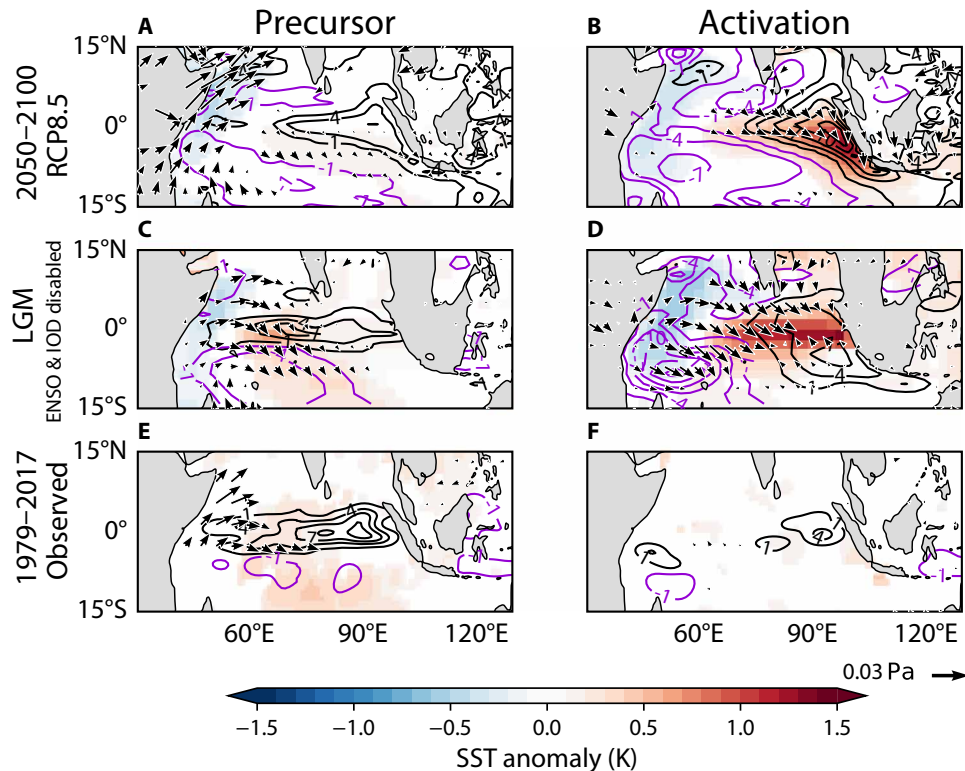


Fig. 3. Atmospheric precursor and developed warm equatorial mode events under greenhouse warming, glacial, and historical conditions. First column: SST (shading), surface wind stress (vectors), and thermocline depth (contours) anomalies associated with the atmospheric precursor of warm equatorial mode (A) in a subset of CMIP5 greenhouse warming simulations, (C) a LGM simulation, and (E) historical observations. Second column: Same as first column but for the peak of the event, 3 months after the occurrence of the precursor. Warm equatorial events are triggered by the atmospheric precursor under (B) greenhouse warming and (D) LGM conditions, but not (F) under historical conditions because the mean state is not conducive for coupled interactions. Events are identified and composited, when the April-May-June standardized zonal wind stress anomalies averaged over the western IO (40°E to 60°E, 2.5°S to 2.5°N) exceeds 0.5. The precursor phase is during May and the peak in August. The LGM simulation has modes of variability disabled as described in the “Methods” section.

At their peak, westerly wind anomalies coupled to the underlying SST gradients span most the basin (Fig. 3, B and D, vectors). These anomalous winds keep the thermocline anomalously deep in the EEIO (Fig. 3, B and D, contours) and suppress equatorial upwelling (not shown) sustaining the positive SSTAs in the EEIO. The pronounced equatorial signature of these events is consistent with the pattern of SST variability increase (Fig. 2, A and B), and their activation occurs under large changes in mean state, such as under LGM conditions (Fig. 2G, red circle), and in the subset of simulations of future climate with the largest increases in variability (Fig. 2G, blue circles with red outline). The changes in mean state also favor the emergence of equatorial cold events with negative SSTAs exhibiting similar magnitude, spatial patterns, and underlying dynamics as the warm events (fig. S5; see Supplementary Text 2). Observations do not show an active mode under current conditions (Fig. 3, E and F, and fig. S5, E and F) because the mean state is not favorable for large-scale coupled interactions (see Supplementary Text 2).

The emergence of the equatorial mode could drive rainfall variability with stronger amplitude and altered patterns over the IO and surrounding land masses relative to currently experienced. Warm

events, with their positive SSTAs spanning much of the equatorial IO, could drive rainfall deficits over the Horn of Africa as well as over Southern India, in addition to increased rainfall over Indonesia and Northern Australia (Fig. 4C). Rainfall anomalies with such patterns and magnitudes have not been observed during the historical period because warm IOD events are extremely weak and their rainfall impacts are restricted to the southeastern IO (Fig. 4A). On the other hand, cold events associated with the equatorial mode could drive rainfall anomalies with a similar spatial pattern and magnitude as the warm events, but with opposite polarity and subtle, yet important differences for terrestrial precipitation (Fig. 4D). For example, cold equatorial events are associated with increased rainfall over peninsular India and thus drive a response opposite to the impacts of a typical cold IOD event (Fig. 4B). These high-amplitude rainfall impacts have only been observed in 1997, during the strongest, cold IOD event on record (11)—the only observed event with SSTAs reaching the EEIO. The emergence of the equatorial mode could make these high-amplitude SSTAs a common occurrence by the second half of the 21st century when CMIP5 models predict two to four events (warm or cold) per decade (range was estimated from

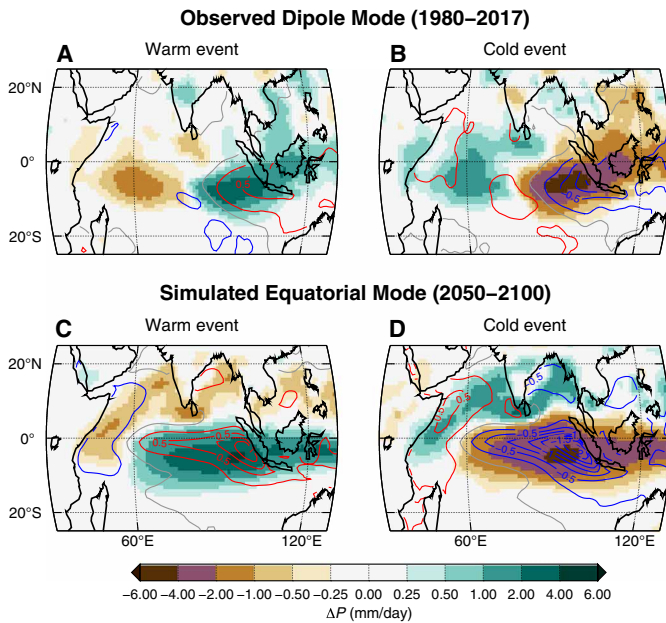


Fig. 4. Rainfall impacts of current and future modes of climate variability in the IO. Composite rainfall anomalies (shading) during (A, B) observed Dipole Mode events and (C, D) simulated Equatorial Mode events active in the IO under greenhouse warming. In both cases, warm (A, C) and cold (B, D) events are, respectively, characterized by positive or negative SST anomalies (contours) over the eastern IO. SST contour interval is 0.25 K. Equatorial Mode events show rainfall and SST anomalies spanning much of the equatorial IO. Anomalies correspond to the peak season of each mode, September–October–November (SON) for the Dipole Mode and August–September–October for the Equatorial Mode. Observed Dipole Mode events are selected and composited on the basis of SON values of the Dipole Mode Index (18) with a 0.5σ threshold. Equatorial Mode events are selected and composited on the basis of indices of the western IO atmospheric precursor and the peak SSTa in the EEIO during the ASO season with a 0.5σ threshold (see “Data” and “Methods” sections). Both criteria combined isolate events that evolve into large-scale SST anomalies. Dipole Mode composites are based on the Global Precipitation Climatology Project (42) and TropFlux (36) observational datasets over the 1980–2017 period. Equatorial Mode composites are based on output from CMIP5 rcp85 simulations over the 2050–2100 period composited for each model run and then averaged across the 10 models with mode activation.

the subset of models with mode activation). Over Sumatra and Java, the associated rainfall fluctuations could represent a surplus (or deficit) of 30 to 50% of current seasonal rainfall during the JAS season. Thus, predicting and attributing changing distributions of future extremes in a warming climate must consider these dynamical changes in rainfall variability alongside with thermodynamic effects (32).

DISCUSSION

In addition to revealing previously unrecognized dynamics of the IO, our results explain the lack of consensus in model predictions of future changes in SST variability in this ocean (9–12). Not all models show increasing SST variability under future greenhouse warming because the equatorial mode does not become active because of muted changes in mean state. Activation might require a change in direction of surface winds along the equator—at least seasonally—so that large-scale upwelling can be established along the equatorial IO. Larger changes rather than just a reversal in winds might be required so that the balance of positive and negative feedbacks in the

EEIO favors unstable growth of SSTAs. Addressing these questions could help clarify the interpretation of model simulations, which show consistent predictions of a strengthening thermocline feedback, yet equivocal results regarding changes in SST variability (9–12). Additional questions must be answered to accurately predict this disruptive outcome, such as whether the changes in the mean state after 2050 will be sufficiently large to favor activation of the equatorial mode. The magnitude of these changes will depend on whether they are amplified by coupled feedbacks, an issue that remains hotly contested (33, 34). All available observational evidence, however, supports predictions of large changes in mean state potentially amplified by coupled feedbacks (fig. S2). Historical observations show pronounced changes in the east-west SST gradient, particularly during the season when coupled feedbacks are stronger (3–5). Here, we showed that only models with equatorial mode activation can simulate changes in the SST gradient as observed (fig. S2). Furthermore, multiple paleoclimate datasets from the LGM show large changes in mean state potentially amplified by coupled feedbacks (24) along with much stronger climate variability (27), attesting to this ocean’s ability to experience large changes in mean state and variability via coupled feedbacks.

In summary, we have demonstrated that the IO can sustain an equatorial mode of climate variability under altered mean states predicted for the second half of the 21st century. This mode manifests as cold and warm interannual events with large-scale SSTAs spanning the central and EEIO. These events, particularly warm ones, represent a marked departure from current variability, characterized by weaker and more spatially confined warm IOD events. Because of their basin-wide and stronger SSTAs, future warm events could drive unprecedented hydrological extremes across the basin. They could bring more frequent droughts to East Africa and southern India, in addition to increased rainfall over Indonesia, exacerbating the effect of a warmer climate on these hydrological extremes (11). Cold and warm events are governed by physical processes similar to those driving El Niño and La Niña and could therefore be predictable at least a season in advance. However, further research on its predictability and global impacts will be needed to improve adaptation efforts to climate change. The emergence of the equatorial mode is supported by a consistent link between changes in variability and mean state across climate models, although a sufficiently large change is required for its activation. These predictions are supported by paleoclimate data from the LGM, which show mean state changes of a magnitude comparable to those predicted under high emissions (24) along with an active equatorial mode (27). Furthermore, the activation of the equatorial mode appears to be less sensitive to common biases in the simulation of seasonal climate by CMIP models (fig. S6 and Supplementary Text 3), supporting our conclusion that this disruptive outcome will be largely determined by the magnitude of the changes in mean state. Further work is needed to accurately assess threshold behavior in this key component of the climate system, particularly under lower-emission scenarios or past climatic states other than the LGM. Present-day conditions do not favor the coupled interactions required for the mode’s emergence, and indeed, historical observations do not show evidence of the occurrence of these extreme events. A potential activation under greenhouse warming, however, could lead to record-breaking SST and rainfall fluctuations, rendering the emergence of the mode a main factor determining future climate risks, including more frequent and devastating wildfires, flooding, and droughts.

MATERIALS AND METHODS**Data**

Our main dataset consists of output from 36 simulations of the 21st-century climate performed with different climate models participating in CMIP5 (35). These simulations were run following the high-emission business as usual Representative Concentration Pathway 8.5 (RCP8.5) scenario, providing an upper bound for the rate and magnitude of global greenhouse warming and associated regional climate changes. We used output from these rcp85 simulations to study changes in the IO mean climate state and variability predicted for the 2050–2100 period. The baseline to assess these changes was obtained from historical simulations performed with the same models under varying natural and anthropogenic radiative forcings over the 1850–2005 period. These simulations were also used to evaluate each model against instrumental observations (see section S2). For each model, one realization, typically member r1i1p1 of the rcp85 and historical simulations, was used in the analysis of mean state and variability changes (e.g., Fig. 2). All available members were used to study the dynamics of the equatorial mode via precursor and composite analysis (e.g., Fig. 3). A total of three members from CESM1-CAM5 and MPI-ESM-LR, two members from FGOALS-s2, and one member from all other models exhibited mode emergence.

The following 36 models with available monthly resolution SST, surface wind stress, rainfall, and subsurface ocean temperature fields from both the rcp85 and historical simulations were included in the analysis: ACCESS1-0, ACCESS1-3, BCC-CSM1.1, BCC-CSM1.1(m), BNU-ESM, CCSM4, CESM1-BGC, CESM1-CAM5, CMCC-CESM, CMCC-CM, CMCC-CMS, CNRM-CM5, CSIRO-Mk3-6-0, FGOALS-s2, FIO-ESM, GFDL-CM3, GFDL-ESM2G, GFDL-ESM2M, GISS-E2-H, GISS-E2-H-CC, GISS-E2-R, GISS-E2-R-CC, HadGEM2-AO, HadGEM2-CC, HadGEM2-ES, INMCM4, IPSL-CM5A-LR, IPSL-CM5A-MR, IPSL-CM5B-LR, MIROC5, MPI-ESM-LR, MPI-ESM-MR, MRI-CGCM3, MRI-ESM1, NorESM1-M, and NorESM1-ME. The CanESM2, MIROC-ESM, and MIROC-ESM-CHEM models were excluded from the final analysis because they exhibit obvious deficiencies in the simulation of the seasonal cycle of key oceanic and atmospheric features in the eastern IO. Further details on this model validation are provided in section S3.

We focused our analysis on the JAS season, when the changes in mean state drive large changes in variability during the subsequent August–September–October season. For each model, we computed changes in ocean and atmospheric mean states as the difference between a given climate variable averaged over July to September during years 2050 to 2100 from the rcp85 simulation minus the corresponding average over years 1850 to 1950 from the historical simulation. Changes in SST variability were quantified by computing the difference between the SD of the detrended SSTAs over the same intervals of the rcp85 and historical simulations. Anomalies were computed as departures from the monthly mean seasonal cycle of each climate variable during the corresponding time interval.

We also analyzed changes in mean state and variability in response to LGM boundary conditions. These changes were computed using simulations performed with CESM1 under LGM and pre-industrial (PI) conditions. The LGM boundary conditions correspond to 21 thousand years before present and include modifications to the following: seasonal and latitudinal insolation, reduced GHG concentrations based on ice core measurements, the effect of a 120-m sea level drop on coastlines and key ocean passages, and the effect of

continental ice sheets (surface albedo and orography) based on the ICE-6GC LGM reconstruction. The implementation of the LGM boundary conditions is fully detailed in previous work studying changes in mean and seasonal climate during this interval (24, 28). The simulation of PI climate was run with external forcings (solar irradiance, GHGs, and land use) set constant to 1850-year values. Our analysis focused on 600 and 500 years of equilibrated climate from each simulation, respectively.

These CESM1 simulations were augmented by a subset of identical LGM and PI simulations in which modes of climate variability influencing the IO were sequentially disabled (table S1). We used these simulations to attribute the processes driving the increase in interannual climate variability seen in the full LGM simulation and ultimately identify the emergence of the equatorial mode presented in this study. The ENSO phenomenon was disabled in a pair of LGM_{XENSO} and PI_{XENSO} simulations by restoring SSTs to their monthly mean seasonal cycle over the equatorial band of the Pacific Ocean (110°E–90°W, 10°N–10°S) computed from the respective LGM and PI simulations. A restoring tendency was applied to the top ocean temperature at every time step during model computation with a damping time scale of 0.5 days. This ensured efficient damping of SSTAs to the climatology of each simulation, preventing the growth of ENSO events in the equatorial Pacific.

The same procedure was applied to an additional pair of LGM_{XENSOXIOD} and PI_{XENSOXIOD} simulations in which both ENSO and the IOD—the leading mode of variability in the modern IO—were disabled. To accomplish this, we applied a restoring temperature tendency over the southeastern IO (95°E to 110°W, 10°S to 2.5°S)—over the center of action of the IOD. SSTs were not restored northward of 2.5°S to allow coupled interactions along the equatorial IO. This procedure effectively removed climate variability associated with the IOD. The PI_{XENSOXIOD} simulation exhibits negligible SST variability over the IO (not shown), confirming that ENSO and the IOD are the main drivers of climate variability under PI conditions. Disabling ENSO also removed variability associated to the IOB mode. These simulations were run for 200 years and used in the analysis in full. No equilibration time was needed because SSTs were restored to the corresponding LGM or PI climatologies over the ENSO and IOD domains.

Multiple observational datasets were used for illustrating key features of modern IO climate and its variability (e.g., Figs. 1 and 3, E and F) as well as validating the CMIP5 simulations (e.g., figs. S1 to S3). Annual mean climate conditions in the equatorial oceans (Fig. 1) were computed from the TropFlux dataset (SST and surface wind stress) (36) and the ORAS4 ocean reanalysis (subsurface ocean temperature) (37) over the common 1979–2017 period. TropFlux and ORAS4 were also used to compute the wind stress and thermocline depth in the EEIO over (fig. S6), as well as the oceanic response to the western IO wind precursor (Fig. 3, E and F). In these cases, TropFlux data over the 1979–2017 period were used. Observed long-term changes in SST discussed in section S1.2 are computed using the following SST reconstructions: HadISST1.1 (38) and versions 3b, 4, and 5 of the Extended Reconstructed Sea Surface Temperature (ERSST3b, ERSST4, and ERSST5) (39–41). Observed rainfall impacts of the IOD (Fig. 4) were computed using version 2.2 of the Global Precipitation Climatology Project dataset (42). Observed IOD events were identified and composited on the basis of the Dipole Mode Index (18) computed using detrended TropFlux SST data. The depth of the thermocline, Z_{TC} , is computed as the location of

the maximum vertical temperature gradient for observations and model simulations. SST, surface wind stress, and Z_{TC} anomalies are computed as departures from their respective monthly mean seasonal cycle. SST variability is quantified by $\sigma(\text{SSTA})$, the SD of the SSTAs. This metric includes variability at all time scales other than seasonal and is typically dominated by interannual variations.

Methods

We used a combination of simulations and diagnostics to isolate the processes driving the pattern of equatorial intensification seen in rcp85 and LGM simulations (Fig. 2, top). The simulations of LGM and PI climate with disabled modes described above and listed in table S1 allowed us to isolate modes of variability as follows. The equatorial mode of variability was isolated by compositing anomalies from the $\text{LGM}_{\text{XENSOXIOD}}$ simulation in which ENSO, the IOD, and other related modes of variability are disabled. The average spatio-temporal evolution of the equatorial mode was studied, compositing anomalies based on an index of SSTA in the EEIO (75°E to 95°E, 2.5°N to 2.5°S). Warm (cold) equatorial mode events were selected for EEIO SSTA larger (less) than 1 (−1) SD during the JAS season. By design, this mode is independent from the IOD and ENSO. We contrasted the evolution of this mode (fig. S3, top) with the IOD (fig. S3, bottom) as follows. IOD events are known to be influenced by ENSO but also occur independently of it (43, 44). Therefore, we computed an IOD composite evolution independent from ENSO using the $\text{LGM}_{\text{XENSO}}$ simulation. We selected warm (cold) events when the dipole index (18) is less (larger) than 1 (−1) SD. By construction, the $\text{LGM}_{\text{XENSO}}$ simulation includes the equatorial mode active in the $\text{LGM}_{\text{NOENSONOIOD}}$. Therefore, we removed the influence of equatorial mode events from the IOD by subtracting the composite anomalies derived from the $\text{LGM}_{\text{XENSOXIOD}}$ simulation from the IOD composite anomalies derived from the $\text{LGM}_{\text{XENSO}}$ simulation.

These composites show that warm equatorial mode and IOD events have different SST and wind stress patterns at their peak (fig. S3, right), as well as different atmospheric precursors (fig. S3, left). Equatorial mode events are preceded by an anomalous surface wind circulation in the western IO and Arabian Sea (fig. S3A, vectors). These anomalous winds have a westerly component over the western equatorial IO, which drive a thermocline deepening along the equatorial IO and initiate the warming over the EEIO. This triggering mechanism is discussed in great detail in the main text (Fig. 3). In contrast, IOD events are preceded by northwesterly wind anomalies over the southeastern side of the basin (along the coast of Java and Sumatra, fig. S3C), consistent with the triggering mechanism of observed IOD events (16, 30, 45).

The peak SST patterns associated with the equatorial mode and the IOD show additional differences. The equatorial mode exhibits peak SSTA concentrated over the EEIO (fig. S3B, shading), whereas the IOD exhibits SST off the coast of Sumatra. Warm IOD events also show SSTA reaching the equator along with westerly wind stress anomalies over the central equatorial IO. This equatorial enhancement of the IOD is likely to be caused by the LGM changes in mean state favoring the growth of SSTA in the EEIO; however, it is much weaker than the SSTAs associated with the equatorial mode. Furthermore, the triggering mechanisms are distinct, confirming that the equatorial mode and the IOD are independent modes.

The analysis of the LGM simulations shows that, while the equatorial mode and the IOD are independent modes of variability, their SST patterns are not entirely orthogonal. This could certainly com-

plicate their isolation in the CMIP5 simulations, particularly under altered mean states when the IOD could exhibit a stronger equatorial imprint. Our analysis of the LGM simulations, however, shows that the equatorial mode is triggered by a distinct atmospheric precursor in the western IO. Therefore, we used this precursor to isolate the equatorial mode in the CMIP5 rcp85 simulations. We focused our analysis on the 2050–2100 period when the changes in mean state and variability are largest. In each model run, we identified equatorial mode events via their atmospheric precursor through an index of zonal wind stress anomalies averaged over the western IO (40°E to 60°E, 5°N to 5°S). We selected precursor events during the April–May–June (AMJ) season when this index is larger (lesser) than (minus) 0.5 SD of the full AMJ-averaged index.

We explored whether and how these wind anomalies trigger large-scale warming (and cooling) events in the EEIO via composite analysis of surface wind stress, SST, and Z_{TC} anomalies on the months and seasons following the atmospheric precursor. This procedure was applied to the subset of 10 rcp85 simulations with strong changes in mean state (Fig. 2G, blue circles with red outline) over the 2050–2100 period. Approximately 10 westerly and 10 easterly precursors were selected from each model run. Composite surface wind stress, SST, and Z_{TC} anomaly maps were produced for the event onset (centered in May) and the event peak (centered in August) for each model (fig. S4). The composite anomalies from all 10 models show the atmospheric precursor in the western IO with westerly wind stress along the equator (fig. S4, left; vectors) and an anomalously deep thermocline to the East (fig. S4, left; contours). All but one model (NorESM1-M) show peak warming in the EEIO 3 months after the AMJ season. The models show that this anomalous warming is associated with an anomalously deep thermocline and westerly winds driven by the underlying SST gradients. Together, these features are indicative of a positive Bjerknes ocean-atmosphere feedback involved in the development of these events. The consistency of this mechanism in all models supports our conclusions that sufficiently large changes in mean state could lead to the activation of the equatorial mode in the IO via stronger coupled interactions in the eastern side of the basin.

We averaged the composite anomalies from each model to produce multimodel ensemble-mean wind stress, SST, and Z_{TC} anomalies for the onset and peak of warm (Fig. 3, A and B) and cold equatorial mode events (fig. S5, A and B). These events show off-equatorial warming (cooling) in the southeastern IO, the center of action of the IOD. However, they do not show alongshore winds as during IOD events, indicating that the coastal warming (cooling) during these events is likely to be forced by coastal Kelvin waves but does not play a role in the development of the equatorial anomalies. Therefore, air-sea coupling in this region is not essential for the growth of equatorial events.

The same procedure was applied to PI simulations (not shown) and available observations (Fig. 3, E and F, and fig. S5, E and F) to seek evidence for an active equatorial mode under current conditions. In both cases, we found that the atmospheric precursor is not followed by large-scale climate anomalies as seen in the LGM and rcp85 simulations, confirming that the equatorial mode is not active under current mean state conditions. Observations do not show evidence for warm equatorial events following westerly wind anomalies in the western IO. In contrast, they show that the easterly wind precursor (fig. S5E) is followed by a weak cooling anomaly off the coast of Java (fig. S5F), consistent with one of the triggering mechanisms of the IOD.

SUPPLEMENTARY MATERIALS

Supplementary material for this article is available at <http://advances.sciencemag.org/cgi/content/full/6/19/eaay7684/DC1>

REFERENCES AND NOTES

- J. H. Christensen, K. Krishna Kumar, E. Aldrian, S.-I. An, I. F. A. Cavalcanti, M. de Castro, W. Dong, P. Goswami, A. Hall, J. K. Kanyanga, A. Kitoh, J. Kossin, N.-C. Lau, J. Renwick, D. B. Stephenson, S.-P. Xie, T. Zhou, *Climate Phenomena and their Relevance for Future Regional Climate Change* (Cambridge Univ. Press, 2013), chap. 14, pp. 1217–1308.
- J. M. Wallace, E. M. Rasmusson, T. P. Mitchell, V. E. Kousky, E. S. Sarachik, H. von Storch, On the structure and evolution of enso-related climate variability in the tropical pacific: Lessons from toga. *J. Geophys. Res. Oceans* **103**, 14241–14259 (1998).
- G. Alory, S. Wijffels, G. Meyers, Observed temperature trends in the Indian Ocean over 1960/1999 and associated mechanisms. *Geophys. Res. Lett.* **34**, L02606 (2007).
- H. Tokinaga, S. Xie, A. Timmermann, S. McGregor, T. Ogata, H. Kubota, Y. M. Okumura, Regional patterns of tropical indo-pacific climate change: Evidence of the walker circulation weakening. *J. Clim.* **25**, 1689–1710 (2012).
- M. K. Roxy, K. Ritika, P. Terray, S. Masson, The curious case of Indian ocean warming. *J. Clim.* **27**, 8501–8509 (2014).
- Y. Du, S.-P. Xie, Role of atmospheric adjustments in the tropical Indian Ocean warming during the 20th century in climate models. *Geophys. Res. Lett.* **35**, L08712 (2008).
- X.-T. Zheng, S.-P. Xie, G. A. Vecchi, Q. Liu, J. Hafner, Indian ocean dipole response to global warming: Analysis of ocean–atmospheric feedbacks in a coupled model. *J. Clim.* **23**, 1240–1253 (2010).
- C. Ihara, Y. Kushnir, M. A. Cane, V. H. de la Peña, Climate change over the equatorial indo-pacific in global warming. *J. Clim.* **22**, 2678–2693 (2009).
- X.-T. Zheng, S. Xie, Y. Du, L. Liu, G. Huang, Q. Liu, Indian ocean dipole response to global warming in the CMIP5 multimodel ensemble. *J. Clim.* **26**, 6067–6080 (2013).
- W. Cai, X.-T. Zheng, E. Weller, M. Collins, T. Cowan, M. Lengaigne, W. Yu, T. Yamagata, Projected response of the Indian Ocean Dipole to greenhouse warming. *Nat. Geosci.* **6**, 999–1007 (2013).
- W. Cai, A. Santoso, G. Wang, E. Weller, L. Wu, K. Ashok, Y. Masumoto, T. Yamagata, Increased frequency of extreme Indian Ocean Dipole events due to greenhouse warming. *Nature* **510**, 254–258 (2014).
- B. Ng, W. Cai, T. Cowan, D. Bi, Influence of internal climate variability on indian ocean dipole properties. *Sci. Rep.* **8**, 13500 (2018).
- N. J. Abram, M. K. Gagan, J. E. Cole, W. S. Hantoro, M. Mudelsee, Recent intensification of tropical climate variability in the Indian Ocean. *Nat. Geosci.* **1**, 849–853 (2008).
- J. E. Tierney, C. C. Ummenhofer, P. B. deMenocal, Past and future rainfall in the Horn of Africa. *Sci. Adv.* **1**, e1500682 (2015).
- K. Thirumalai, P. N. DiNezio, Y. Okumura, C. Deser, Extreme temperatures in Southeast Asia caused by El Niño and worsened by global warming. *Nat. Commun.* **8**, 15531 (2017).
- R. Murtugudde, J. P. McCreary Jr., A. J. Busalacchi, Oceanic processes associated with anomalous events in the Indian Ocean with relevance to 1997–1998. *J. Geophys. Res. Oceans* **105**, 3295–3306 (2000).
- C. Birkett, R. Murtugudde, T. Allan, Indian Ocean climate event brings floods to East Africa's lakes and the Sudd Marsh. *Geophys. Res. Lett.* **26**, 1031–1034 (1999).
- N. H. Saji, B. N. Goswami, P. N. Vinayachandran, T. Yamagata, A dipole mode in the tropical Indian Ocean. *Nature* **401**, 360–363 (1999).
- F.-F. Jin, Tropical ocean–atmosphere interaction, the pacific cold tongue, and the el niño–southern oscillation. *Science* **274**, 76–78 (1996).
- S. A. Klein, B. J. Soden, N.-C. Lau, Remote sea surface temperature variations during ENSO: Evidence for a tropical atmospheric bridge. *J. Clim.* **12**, 917–932 (1999).
- N.-C. Lau, M. J. Nath, Atmosphere–ocean variations in the indo-pacific sector during ENSO episodes. *J. Clim.* **16**, 3–20 (2003).
- F. A. Schott, S.-P. Xie, J. P. McCreary Jr., Indian Ocean circulation and climate variability. *Rev. Geophys.* **47**, RG1002 (2009).
- W. Cai, L. Wu, M. Lengaigne, T. Li, S. M. Gregor, J. S. Kug, J. Y. Yu, M. F. Stuecker, A. Santoso, X. Li, Y. G. Ham, Y. Chikamoto, B. Ng, M. J. M. Phaden, Y. Du, D. Dommenget, F. Jia, J. B. Kajtar, N. Keenlyside, X. Lin, J. J. Luo, M. Martin-Rey, Y. Ruprich-Robert, G. Wang, S. P. Xie, Y. Yang, S. M. Kang, J. Y. Choi, B. Gan, G. I. Kim, C. E. Kim, S. Kim, J. H. Kim, P. Chang, Pantropical climate interactions. *Science* **363**, eaav4236 (2019).
- P. N. DiNezio, J. E. Tierney, B. L. Otto-Bliesner, A. Timmermann, T. Bhattacharya, N. Rosenbloom, E. Brady, Glacial changes in tropical climate amplified by the indian ocean. *Sci. Adv.* **4**, eaat9658 (2018).
- G. Windler, J. E. Tierney, P. N. DiNezio, K. Gibson, R. Thunell, Shelf exposure influence on Indo-Pacific Warm Pool climate for the last 450,000 years. *Earth Planet. Sci. Lett.* **516**, 66–76 (2019).
- J. W. Hurrell, M. M. Holland, P. R. Gent, S. Ghan, J. E. Kay, P. J. Kushner, J. Lamarque, W. G. Large, D. Lawrence, K. Lindsay, W. H. Lipscomb, M. C. Long, N. Mahowald, D. R. Marsh, R. B. Neale, P. Rasch, S. Vavrus, M. Vertenstein, D. Bader, W. D. Collins, J. J. Hack, J. Kiehl, S. Marshall, The community earth system model: A framework for collaborative research. *Bull. Am. Meteorol. Soc.* **94**, 1339–1360 (2013).
- K. Thirumalai, P. N. DiNezio, J. E. Tierney, M. Puy, M. Mohtadi, An El Niño mode in the glacial indian ocean? *Paleoceanogr. Paleoclimatol.* **34**, 1316–1327 (2019).
- P. N. DiNezio, A. Timmermann, J. E. Tierney, F.-F. Jin, B. Otto-Bliesner, N. Rosenbloom, B. Mapes, R. Neale, R. F. Ivanovic, A. Montenegro, The climate response of the Indo-Pacific warm pool to glacial sea level. *Paleoceanography* **31**, 866–894 (2016).
- P. J. Webster, A. M. Moore, J. P. Loschnigg, R. R. Leben, Coupled ocean–atmosphere dynamics in the Indian Ocean during 1997–98. *Nature* **401**, 356–360 (1999).
- R. Murtugudde, A. J. Busalacchi, Interannual variability of the dynamics and thermodynamics of the tropical indian ocean. *J. Clim.* **12**, 2300–2326 (1999).
- J. Bjerknes, Atmospheric teleconnections from the equatorial pacific. *Mon. Weather Rev.* **97**, 163–172 (1969).
- S. Pfahl, P. A. O’Gorman, E. M. Fischer, Understanding the regional pattern of projected future changes in extreme precipitation. *Nat. Clim. Chang.* **7**, 423–427 (2017).
- G. Li, S.-P. Xie, Y. Du, A robust but spurious pattern of climate change in model projections over the tropical Indian ocean. *J. Clim.* **29**, 5589–5608 (2016).
- G. Wang, W. Cai, A. Santoso, Assessing the impact of model biases on the projected increase in frequency of extreme positive Indian ocean dipole events. *J. Clim.* **30**, 2757–2767 (2017).
- K. E. Taylor, R. J. Stouffer, G. A. Meehl, An overview of cmip5 and the experiment design. *Bull. Am. Meteorol. Soc.* **93**, 485–498 (2012).
- B. P. Kumar, J. Vialard, M. Lengaigne, V. S. N. Murty, M. J. McPhaden, M. F. Cronin, F. Pinsard, K. G. Reddy, Tropflux wind stresses over the tropical oceans: evaluation and comparison with other products. *Clim. Dyn.* **40**, 2049–2071 (2013).
- M. A. Balmaseda, K. Mogensen, A. T. Weaver, Evaluation of the ECMWF ocean reanalysis system ORAS4. *Q. J. R. Meteorol. Soc.* **139**, 1132–1161 (2013).
- N. A. Rayner, D. E. Parker, E. B. Horton, C. K. Alexander, L. V. Alexander, D. P. Rowell, E. C. Kent, A. Kaplan, Global analyses of sea surface temperature, sea ice, and night marine air temperature since the late nineteenth century. *J. Geophys. Res. Atmos.* **108**, 4407 (2003).
- T. M. Smith, R. W. Reynolds, T. C. Peterson, J. Lawrimore, Improvements to noaa’s historical merged land–ocean surface temperature analysis (1880–2006). *J. Clim.* **21**, 2283–2296 (2008).
- B. Huang, V. F. Banzon, E. Freeman, J. Lawrimore, W. Liu, T. C. Peterson, T. M. Smith, P. W. Thorne, S. D. Woodruff, H. Zhang, Extended reconstructed sea surface temperature version 4 (ERSST.v4). Part I: Upgrades and intercomparisons. *J. Clim.* **28**, 911–930 (2015).
- B. Huang, P. W. Thorne, V. F. Banzon, T. Boyer, G. Chepurin, J. H. Lawrimore, M. J. Menne, T. M. Smith, R. S. Vose, H. Zhang, Extended reconstructed sea surface temperature, version 5 (ersst.v5): Upgrades, validations, and intercomparisons. *J. Clim.* **30**, 8179–8205 (2017).
- G. J. Huffman, D. T. Bolvin, E. J. Nelkin, R. F. Adler, GPCP Version 2.2 Combined Precipitation Data Set (2015).
- D. Dommenget, An objective analysis of the observed spatial structure of the tropical indian ocean sst variability. *Clim. Dyn.* **36**, 2129–2145 (2011).
- M. F. Stuecker, A. Timmermann, F.-F. Jin, Y. Chikamoto, W. Zhang, A. T. Wittenberg, E. Widiasih, S. Zhao, Revisiting ENSO/Indian Ocean Dipole phase relationships. *Geophys. Res. Lett.* **50**, 2305 (2017).
- H. Annamalai, R. Murtugudde, J. Potemra, S. P. Xie, P. Liu, B. Wang, Coupled dynamics over the indian ocean: Spring initiation of the zonal mode. *Deep-Sea Res. II Top. Stud. Oceanogr.* **50**, 2305–2330 (2003).
- B. Praveen Kumar, J. Vialard, M. Lengaigne, V. S. N. Murty, M. J. McPhaden, TropFlux: Air-sea fluxes for the global tropical oceans—description and evaluation. *Clim. Dyn.* **38**, 1521–1543 (2011).
- N. H. Saji, S.-P. Xie, T. Yamagata, Tropical indian ocean variability in the ipcc twentieth-century climate simulations. *J. Clim.* **19**, 4397–4417 (2006).
- W. Cai, A. Sullivan, T. Cowan, J. Ribbe, G. Shi, Simulation of the indian ocean dipole: A relevant criterion for selecting models for climate projections. *Geophys. Res. Lett.* **38**, L03704 (2011).
- L. Liu, W. Yu, T. Li, Dynamic and thermodynamic air–sea coupling associated with the indian ocean dipole diagnosed from 23 WCRP CMIP3 models. *J. Clim.* **24**, 4941–4958 (2011).
- E. Weller, W. Cai, Realism of the indian ocean dipole in cmip5 models: The implications for climate projections. *J. Clim.* **26**, 6649–6659 (2013).
- S.-P. Xie, K. Hu, J. Hafner, H. Tokinaga, Y. Du, G. Huang, T. Sampe, Indian ocean capacitor effect on indo–western pacific climate during the summer following el niño. *J. Clim.* **22**, 730–747 (2009).
- G. Li, S.-P. Xie, Tropical biases in cmip5 multimodel ensemble: The excessive equatorial pacific cold tongue and double itcz problems. *J. Clim.* **27**, 1765–1780 (2014).

Acknowledgments: We thank J. Partin for comments on this work. We wish to acknowledge members of NCAR’s Climate Modeling Section, the CESM Software Engineering Group (CSEG), and the Computation and Information Systems Laboratory (CISL) for their contributions to the development of CESM. **Funding:** Funding for this work was provided by UTIG (to M.P.), NSF (grant OCN–1903478 to P.D.N. and grant OCE–1903482 to K.T.), the Brown Presidential

Fellowship (to K.T.), and the David and Lucile Packard Foundation (to J.E.T.). **Author contributions:** P.D.N. and M.P. conceived the study. M.P. performed the analysis. P.D.N. wrote the manuscript. All authors contributed to the analysis and interpretation of the results. **Competing interests:** The authors declare that they have no competing interests. **Data and materials availability:** All data needed to evaluate the conclusions in the paper are present in the paper and/or the Supplementary Materials. Additional data related to this paper may be requested from the authors.

Submitted 16 July 2019
Accepted 25 February 2020
Published 6 May 2020
10.1126/sciadv.aay7684

Citation: P. N. DiNezio, M. Puy, K. Thirumalai, F.-F. Jin, J. E. Tierney, Emergence of an equatorial mode of climate variability in the Indian Ocean. *Sci. Adv.* **6**, eaay7684 (2020).